Energy-efficient Controller Design for a Redundantly-actuated Hybrid Feed Drive with Application to Machining

Molong Duan, *Student Member, IEEE,* Chinedum E. Okwudire, *Member, IEEE*

***Abstract*— This paper presents a method for designing a controller that achieves the best positioning performance while maximizing the energy efficiency of a redundantly-actuated hybrid feed drive. A two degree-of-freedom controller, consisting of a feed forward (FF) controller for tracking and a feedback (FB) controller for regulation, is assumed. It is shown that the ideal FF controller, which achieves perfect tracking with maximum efficiency, is not always stable. Therefore, a method for designing a stable FF controller that achieves perfect tracking with near optimal efficiency is proposed. Furthermore, the optimal relationship between FB control inputs, which guarantees maximum efficiency for any specified regulation performance, is derived. Two approaches for using the derived optimal relationship to synthesize a FB controller that achieves the best positioning performance while maximizing efficiency are proposed. Simulations and machining experiments are conducted to demonstrate the effectiveness of the proposed energy-efficient FF and FB controller design methods. Significant improvements in energy efficiency (without sacrificing positioning performance) are reported.**

***Index Terms*— Energy Efficiency; Control Structure Design; H_2/H_∞ Optimization; Hybrid Feed Drive; Redundant Actuation**

I. Introduction

Feed drives are used for coordinated motion delivery in manufacturing machines. Consequently, their positioning accuracy and speed are critical to the quality and productivity of a variety of manufacturing processes [1]. Moreover, they account for a significant portion of the energy consumption of manufacturing machines [2], [3]. Therefore, a lot of work has been done in the literature related to improving their energy efficiency, e.g., [4]–[10]. It is however recognized that, to achieve truly sustainable manufacturing, improvements in energy efficiency must be achieved without unduly sacrificing quality and productivity [11].

Most machine tools utilize screw drives (SDs) for actuating their feed axes [1]. The reason is that SDs are cost effective and have high mechanical advantage which allows them to support high cutting (i.e., machining) forces with very low energy consumption [12], [13]. The speed and accuracy of SDs are however limited because of mechanical issues like vibration, wear, backlash and geometric errors of the screw and associated mechanical components [1], [13]. To mitigate these shortcomings, linear motor drives (LMDs) are increasingly being resorted to [13]–[18]. LMDs can achieve higher speeds and accelerations than SDs and are not subject to the inaccuracies caused by geometric errors, wear and structural deformations arising from the screw and other mechanical components like bearings, couplers and nuts that are connected to it [1], [13]. LMDs are therefore generally more precise than SDs. However, because they provide no mechanical advantage, they consume a lot more electrical energy to support cutting forces than SDs, thus significantly increasing the energy consumption of the machine [15].

When two or more actuators provide complementary benefits (as in SDs and LMDs), it is not uncommon to resort to hybrid feed drives (HFDs). In HFDs, dissimilar but complementary actuators are synergistically combined to meet conflicting requirements with little or no tradeoff. HFDs are most commonly designed with actuators that act in series to achieve long-range coarse motion and short-range fine motion, thus improving positioning speed and precision [19]–[24]. A relatively uncommon configuration of HFDs is the parallel HFD, where two dissimilar actuators are coupled together in parallel. For example, Shinno et al. [25] developed a tilting platform consisting of a pneumatic actuator and a couple of voice coil motors, in order to simultaneously generate high-precision and high-torque motions. Frey et al. [26] proposed a parallel HFD consisting of an SD and an LMD, which was controlled to actively damp the axial vibration of the SD. Okwudire and Rodgers [27] proposed a parallel HFD which synergistically combined an LMD and an SD to achieve speeds and accuracies similar to LMDs while consuming up to 80% less energy [27], [28]. However, the controller design technique they employed was ad hoc and could not guarantee that the best positioning performance and/or energy efficiency was achieved.

Well-established controller design techniques, like LQR [5] and mixed sensitivity H_2/H_∞ synthesis [29], can be employed to systematically design energy optimal controllers. Such techniques depend on user-defined weighting functions or matrices which are used to trade off conflicting requirements (e.g., positioning performance and energy efficiency) [5], [29], [30]. However, the methods do not provide a clear means of

Manuscript received on February 6, 2015. This work is funded by the National Science Foundation's CAREER Award #1350202: Dynamically Adaptive Feed Drives for Smart and Sustainable Manufacturing.

M. Duan and C.E. Okwudire are with University of Michigan, Ann Arbor, MI 48109 USA. (e-mail: molong@umich.edu; okwudire@umich.edu).

ensuring that the selected weighting filters/matrices provide the best tradeoff, especially when applied to redundantly-actuated systems, like HFDs, for which it is desired to have little or no tradeoff. This paper presents a systematic methodology for designing a controller that achieves the best positioning performance while maximizing the energy efficiency of a redundantly-actuated parallel HFD. Specifically, it proposes a near energy optimal feed forward controller for perfect tracking; it also proposes a means of determining the best feedback gain structure (or weighting filter) to use in H_2/H_∞ controller synthesis in order to achieve maximum energy efficiency. Section II gives a brief overview of a parallel HFD and presents a model for its low-order dynamics and actuator efficiency. In Section III, details of the proposed energy-efficient controller design methodology are provided. Comparative simulations and experiments are reported in Section IV to evaluate the effectiveness of the proposed technique, followed by discussions, conclusions and future work.

II. Overview and Modeling of Hybrid Feed Drive

A. Overview of Hybrid Feed Drive (HFD)

Machining operations typically consist of a combination of two modes – rapid traverse (i.e., high-speed, zero-cutting-force positioning moves) and cutting, usually involving low feed rates and large cutting forces. The idea behind the HFD is to: (*i*) drive the machine table using the LMD during rapid traverse to achieve very high speeds and accelerations with low energy consumption; (*ii*) drive the table using a low-lead SD during cutting to achieve the required cutting speeds with low energy consumption; (*iii*) use the LMD to compensate for vibrations and errors introduced by the SD during cutting; and (*iv*) ensure that the switch between the LMD and SD can be achieved rapidly and energy efficiently at any position of the table within its travel.

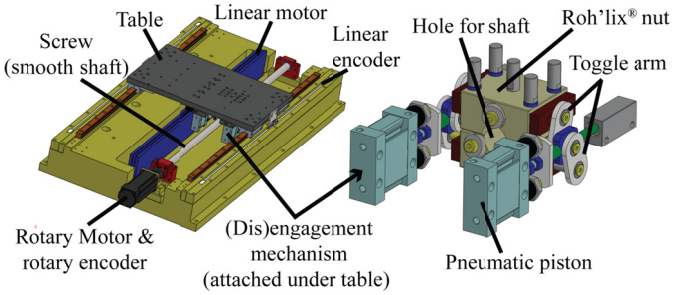

Fig. 1. Schematic of HFD Prototype Proposed by Okwudire and Rogers [10]

Fig. 1 shows the schematic of a HFD prototype whose design is detailed by Okwudire and Rogers [27]. An air core linear motor is employed to drive the table, because it does not need to support large cutting forces for which iron core motors are better suited. The SD is driven by a brushless DC motor. The HFD is equipped with a 0.08 μm resolution optical linear encoder fixed to one side of the table, and a 157 μrad resolution motor-mounted optical rotary encoder.

To facilitate easy engagement and disengagement of the SD from the table, a traction drive SD which uses a rolling helix (or Roh'lix®) nut [31], [32] is employed. The Roh'lix nut converts rotary motion to linear motion using rolling element ball bearings that trace a screw motion (of lead = 5 mm) along a smooth shaft of 25 mm diameter and 965 mm length. It is designed to carry up to 444 N of thrust force without slippage between the nut and shaft. The Roh'lix nut consists of two spring-loaded halves that can be separated to disengage the smooth shaft from the nut at any given location. A simple toggle mechanism is designed to separate the two halves of the nut using a pair of fast-acting pneumatic pistons. The HFD thus has two modes – (*i*) the rapid traverse mode, when the nut is disengaged from the shaft and the LMD acts alone; and (*ii*) the cutting mode, when the nut is engaged to the shaft, allowing the SD and LMD to work together in parallel to actuate the table. This paper is focused on the design of a controller for optimal control effort allocation to the LMD and SD during the cutting mode.

B. Modeling of HFD Dynamics and Actuator Efficiency

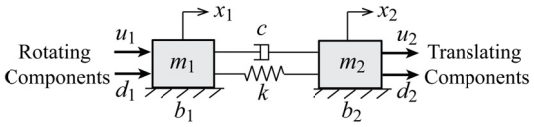

Fig. 2. Simple Two-mass Model of HFD

A simple two-mass model (like the one shown in Fig. 2 for the HFD) is commonly used to analyze the mechanical dynamics of SDs for control purposes [33]–[36]. Even though more advanced SD models are available in the literature (e.g., [37]), the two-mass model is preferred because it is simple and it captures the first axial/torsional vibration mode, which is well known to be the bottleneck for controller design for SDs [33]–[36]. The LMD does not add any new low-order mechanical dynamics to the HFD shown in Fig. 1. Therefore, the two-mass model used for SDs can also be used for controller design and analysis of the HFD [26].

In the two-mass model of Fig. 2, m_1 and m_2 are the (equivalent) masses of the rotating and translating components of the HFD, while k and c represent the stiffness and viscous damping coefficient of the connecting mechanical components; x_1, x_2 and b_1, b_2 are the (equivalent) displacements and viscous damping coefficients at m_1 and m_2, respectively; u_1 and u_2 are the (equivalent) control forces applied by the rotary and linear motors, while d_1 and d_2 represent external disturbance forces (e.g., non-viscous friction and cutting forces) applied to m_1 and m_2, respectively. The equation of motion of the HFD is given by

$$\begin{aligned} m_1\ddot{x}_1 + b_1\dot{x}_1 + c(\dot{x}_1 - \dot{x}_2) + k(x_1 - x_2) &= u_1 + d_1, \\ m_2\ddot{x}_2 + b_2\dot{x}_2 + c(\dot{x}_2 - \dot{x}_1) + k(x_2 - x_1) &= u_2 + d_2. \end{aligned} \tag{1}$$

Defining s as the Laplace variable, the plant transfer function matrix, $\mathbf{G}$, between the input forces, $\mathbf{u} = \{u_1, u_2\}^T$ and $\mathbf{d} = \{d_1, d_2\}^T$, and the output displacements, $\mathbf{x} = \{x_1, x_2\}^T$, of the HFD is derived as

$$\mathbf{x}(s) = \underbrace{\begin{bmatrix} G_{11}(s) & G_{12}(s) \\ G_{21}(s) & G_{22}(s) \end{bmatrix}}_{\mathbf{G}(s)} \big(\mathbf{u}(s) + \mathbf{d}(s)\big), \tag{2}$$

where

$$G_{11}=\frac{m_2s^2+(c+b_2)s+k}{D_{ol}},\quad G_{22}=\frac{m_1s^2+(c+b_1)s+k}{D_{ol}},$$
$$G_{12}=G_{21}=\frac{cs+k}{D_{ol}},\quad D_{ol}=a_{ol,4}s^4+a_{ol,3}s^3+a_{ol,2}s^2+a_{ol,1}s; \tag{3}$$
$$a_{ol,4}=m_1m_2;\quad a_{ol,3}=b_1m_2+b_2m_1+c(m_1+m_2)$$
$$a_{ol,2}=c(b_1+b_2)+k(m_1+m_2)+b_1b_2;\quad a_{ol,1}=(b_1+b_2)k.$$

The energy efficiency of electric motors (linear or rotary) is adversely affected by copper losses, iron losses, friction, and switching losses in the motors and their amplifiers [2][10]. Of these loss mechanisms, copper losses (i.e., I^2R losses) are by far the most dominant, especially at high loads [2], which are typical in machining. Therefore, in this paper, the heat energy generated as a result of copper losses is used as a measure of actuator efficiency. It is given by the equation [5]–[10]

$$E_{heat}=\sum_{i=1}^{2}\int\left(\frac{u_i}{K_{mi}}\right)^2 dt\ . \tag{4}$$

The parameter K_{mi} represents the (equivalent) motor constant of the ith actuator in N/$\sqrt{\text{W}}$. It is often reported in the specification sheets of electric motors. Given the same RMS actuation force, the motor constant provides a measure of the comparative efficiency of each actuator; the larger the motor constant, the more efficient the motor. Note that the motor constant for rotary motors is typically provided in units of Nm/$\sqrt{\text{W}}$; it is converted to N/$\sqrt{\text{W}}$ using a factor of $2\pi/l$, where l represents the lead of the screw in meters.

III. Proposed HFD Controller Design Methodology

In motion control applications, it is common to use a so-called two degree-of-freedom (DOF) structure, consisting of a feed forward (FF) and feedback (FB) controller. The FF controller focuses on tracking reference commands while the FB controller handles regulation tasks. The 2-DOF control structure for the HFD is shown in Fig. 3. The FF controller, $\mathbf{C}_{ff}$, takes the desired position trajectory x_d as its input and generates the FF component, $\mathbf{u}_{ff} = \{u_{ff1}\ u_{ff2}\}^{\mathrm{T}}$, of the control signal $\mathbf{u}$, as well as the reference position signal, $\mathbf{x}_r = \{x_{r1}\ \ x_{r2}\}^{\mathrm{T}}$, for the feedback controller. On the other hand, the FB controller, $\mathbf{C}_{fb}$, determines the feedback component, $\mathbf{u}_{fb} = \{u_{fb1}\ u_{fb2}\}^{\mathrm{T}}$, of $\mathbf{u}$ based on the error vector, $\mathbf{e} = \mathbf{x}_r - \mathbf{x}$. It is of interest to design $\mathbf{C}_{ff}$ and $\mathbf{C}_{fb}$ such that:

(*a*) The best positioning performance is achieved, subject to stability constraints; and

(*b*) Specification (*a*) above is achieved as energy efficiently as possible (i.e., with minimal heat loss from the actuators).

The underlying assumption in defining the two-tiered specifications above is that, in precision machining, positioning performance typically takes precedence over energy efficiency. Therefore, as much as possible, positioning performance should not be sacrificed for energy efficiency. It is assumed that, because of the redundant actuation of the HFD, there are multiple combinations of u_1 and u_2 that can achieve the best positioning performance; of those, the most efficient should be selected. An elegant methodology for achieving the stated goals by properly designing $\mathbf{C}_{ff}$ and $\mathbf{C}_{fb}$ is proposed in the following two subsections.

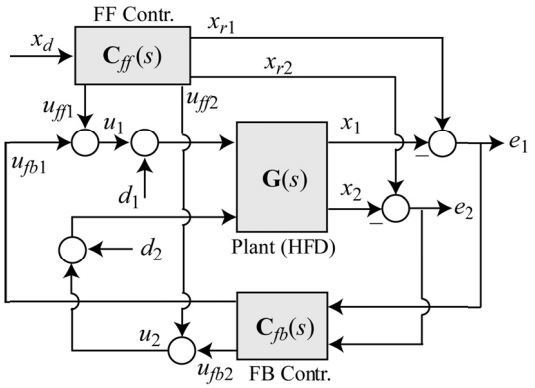

Fig. 3. Block Diagram of Two-DOF Control Structure for HFD

A. Design of Energy-efficient FF Controller

Let us consider the tracking problem, where $\mathbf{d}$ is ignored and $\mathbf{u}_{fb} = \mathbf{0}$ such that $\mathbf{u} = \mathbf{u}_{ff}$. The machine tool is provided with a desired position trajectory $x_d(t)$ to follow (where t represents time). The best FF positioning performance is for the position of the table, x_2, to perfectly track x_d, i.e., $x_d - x_2 = 0$. Note that the motor shaft position, x_1, needs not follow x_d. Accordingly, we define $x_{r2} = x_d$ as the reference command to the HFD's table, so that the perfect tracking constraint boils down to the condition $x_2 = x_{r2} = x_d$. Assuming that the HFD's dynamics is accurately modeled by its two-mass model, $\mathbf{G}$, the following condition holds true under perfect tracking:

$$\begin{Bmatrix} x_{r1} \\ x_d \end{Bmatrix} = \begin{bmatrix} G_{11} & G_{12} \\ G_{21} & G_{22} \end{bmatrix} \begin{Bmatrix} u_{ff1} \\ u_{ff2} \end{Bmatrix}.$$
$$\therefore x_d = G_{21}u_{ff1} + G_{22}u_{ff2} \Rightarrow G_{21}\delta u_{ff1} + G_{22}\delta u_{ff2} = 0. \tag{5}$$

The operator δ represents the variation of a function or functional [38]; $\delta x_d = 0$ because x_d is a specified function of time.

The most energy efficient FF controller must generate $\mathbf{u}_{ff}$ to minimize objective functional

$$\int\left(\left(\frac{u_{ff1}}{K_{m1}}\right)^2+\left(\frac{u_{ff2}}{K_{m2}}\right)^2\right)dt, \tag{6}$$

which represents the heat dissipated in both actuators of the HFD based on (4). The functional is minimized when its variation is zero [38]; i.e.,

$$\int\left(\frac{2u_{ff1}}{K_{m1}^{\ 2}}\delta u_{ff1}+\frac{2u_{ff2}}{K_{m2}^{\ 2}}\delta u_{ff2}\right)dt = 0$$
$$\Rightarrow \frac{\delta u_{ff2}}{\delta u_{ff1}}\kappa^2 = -\frac{u_{ff1}}{u_{ff2}}, \tag{7}$$

where $\kappa = K_{m1}/K_{m2}$. Combining (7) with the perfect tracking constraint of (5) gives the energy optimal FF control law as

$$u_{ff1} = \kappa^2 G_{22}^{\ -1}G_{21}u_{ff2},\quad u_{ff2} = G_{ff}^{-1}x_d;$$
$$G_{ff} \triangleq \kappa^2 G_{22}^{\ -1}G_{21}^2 + G_{22}. \tag{8}$$

Accordingly, x_{r1} is given by

$$x_{r1} = G_{11}u_{ff1} + G_{12}u_{ff2} = \left(\kappa^2 G_{11}G_{22}^{-1}G_{21} + G_{12}\right)G_{ff}^{-1}x_d. \quad (9)$$

One major challenge that arises with the energy optimal FF controller (given by (8)) is that, even though each element of **G** is minimum phase, the transfer function G_{ff} may have non-minimum phase (NMP) zeros, as such, it may not have a stable inverse. There are several methods in the literature for calculating a stable approximation for the inverse for a transfer function with NMP zeros (e.g., [39]–[41]). Amongst them, the most notable is Tomizuka's zero phase error tracking control (ZPETC) [39]. ZPETC determines a stable inverse such that there are no errors in phase across all frequencies; however, it gives rise to errors in gain compared to the exact inverse. If the numerator and denominator polynomials of G_{ff} are represented by B_{ff} and A_{ff}, respectively, its stable inverse with zero phase error is given by

$$G_{ff-zpetc}^{-1} = \frac{A_{ff}(s)B_{ffu}(-s)}{B_{ffs}(s)B_{ffu}^2(0)}, \quad (10)$$

where B_{ffs} and B_{ffu} represent the stable and unstable portions of B_{ff}. Note that (10) represents the continuous-time equivalent of Tomizuka's discrete-time ZPETC [39].

The problem with the approximate inverse of (10) is that it sacrifices energy optimality as well as perfect tracking because it satisfies neither (5) nor (7); this is also the case for the other similar approximate inversion methods available in the literature (e.g., [40], [41]). We therefore seek a minimum phase approximation for G_{ff} that can guarantee perfect tracking while maintaining near energy optimality. To determine such a near energy optimal (NEO) FF controller, let the minimum energy condition of (7) be re-written as

$$\frac{\delta u_{ff2}}{\delta u_{ff1}}\kappa^2 = -\frac{u_{ff1}}{u_{ff2}} + K_{ff}, \quad (11)$$

where K_{ff} is a gain. The implication of (11) is that energy optimality is sacrificed by making the variation of the energy functional in (7) to be non-zero by introducing K_{ff}. Combining the perfect tracking constraint of (5) with (11), we get

$$u_{ff1} = \left(K_{ff} + \kappa^2 G_{22}^{-1}G_{21}\right)u_{ff2}, \quad u_{ff2} = G_{ff-neo}^{-1}x_d; \quad G_{ff-neo} \triangleq G_{21}K_{ff} + \kappa^2 G_{22}^{-1}G_{21}^2 + G_{22}. \quad (12)$$

It can be shown that there always exists a $K_{ff} \in [0, \infty)$ that makes G_{ff-neo} to be minimum phase. To do this, let us re-write G_{ff-neo} as

$$G_{ff-neo} = G_{22}^{-1}\left(G_{22}G_{21}K_{ff} + \kappa^2 G_{21}^2 + G_{22}^2\right). \quad (13)$$

Therefore, the zeros of G_{ff-neo} can be obtained from the the roots of the polynomial

$$\text{num}\left(G_{22}G_{21}\right)K_{ff} + \kappa^2\text{num}\left(G_{21}^2\right) + \text{num}\left(G_{22}^2\right), \quad (14)$$

where num is a function that returns the numerator of the transfer function in its argument. Notice that (14) is in the standard form for root locus analysis. When $K_{ff} = 0$, the zeros of G_{ff-neo} are the same as those of G_{ff}. However, as $K_{ff} \to \infty$, the zeros of G_{ff-neo} approach the zeros of $G_{22}G_{21}$ which, according to (3), are always minimum phase. Since the objective functional of (6) is quadratic, near optimality is achieved by selecting the smallest value of K_{ff} that makes the poles of G^{-1}_{ff-neo} stable, and provides sufficient damping to prevent ringing due to poorly damped poles [39]. Note that if G_{ff} is minimum phase, $K_{ff} = 0$ becomes the default solution for K_{ff}, in which case G_{ff-neo} equals G_{ff}, which is the energy optimal solution. Given K_{ff}, x_{r1} can be calculated as

$$x_{r1} = G_{11}u_{ff1} + G_{12}u_{ff2} = \left(G_{11}\left(K_{ff} + \kappa^2 G_{22}^{-1}G_{21}\right) + G_{12}\right)G_{ff-neo}^{-1}x_d. \quad (15)$$

B. Design of Energy-efficient FB Controller

For the regulation problem, $\mathbf{x}_r$ and $\mathbf{u}_{ff}$ are ignored such that $\mathbf{u} = \mathbf{u}_{fb}$ can be written as

$$\mathbf{u}_{fb} = -\mathbf{K}\mathbf{z}, \quad (16)$$

where $\mathbf{z}$ is the extended state vector of the HFD defined as

$$\mathbf{z} = \left\{x_{2i} \quad x_1 \quad x_2 \quad \dot{x}_1 \quad \dot{x}_2\right\}^{\mathrm{T}}; \; x_{2i} \triangleq \int x_2 dt\,. \quad (17)$$

Observe that $\mathbf{z}$ contains all four states of the two-mass model of the HFD, plus an additional state, x_{2i}, representing the integral of the table's position signal, added to ensure zero steady-state regulation of the table's position. Let us assume that **K** is a full state FB matrix which can be expressed as

$$\mathbf{K} = \begin{bmatrix} K_{11} & K_{12} & K_{13} & K_{14} & K_{15} \\ K_{21} & K_{22} & K_{23} & K_{24} & K_{25} \end{bmatrix}, \quad (18)$$

where $K_{11}\ldots K_{25}$ are its gains. This means that the general form of $\mathbf{C}_{fb}$, indicated in Fig. 3, can be written as

$$\mathbf{C}_{fb}(s) = \begin{bmatrix} K_{12} + K_{14}s & K_{11}/s + K_{13} + K_{15}s \\ K_{22} + K_{24}s & K_{21}/s + K_{23} + K_{25}s \end{bmatrix}. \quad (19)$$

In the rest of this section, we will show that there always exists some redundancy in the general form of $\mathbf{C}_{fb}$, in terms of achieving the best FB positioning performance. We therefore propose a systematic method for using the available redundancy to maximize actuator efficiency without sacrificing positioning performance.

1) Redundancy in Achieving Best Positioning Performance

Recall that it is the precise positioning of the table (i.e., x_2) that is of primary concern for the HFD. Therefore, the goal of the FB controller is to minimize the effect of disturbance **d** on e_2. This objective can be written as

$$\min J \triangleq \left\|W_e\mathbf{S}_d\right\| \text{ s.t. stability constraints}, \quad (20)$$

where $\|\cdot\|$ represents a suitable norm (e.g., H_2 or H_∞), W_e is a scalar weighting function of s that indicates the frequencies in e_2 that are of utmost importance, and $\mathbf{S}_d$ is defined as a scaled version of the closed loop (CL) disturbance transfer function from **d** to e_2, given by the expression

$$\mathbf{S}_d = -\begin{bmatrix}0 & 1\end{bmatrix}\left(\mathbf{I} + \mathbf{G}\mathbf{C}_{fb}\right)^{-1}\mathbf{G}\mathbf{W}_d, \quad (21)$$

where **I** is the identity matrix and $\mathbf{W}_d = \text{diag}(\{d_{1,\max}, d_{2,\max}\})$ is a matrix that scales d_1 and d_2 by their respective maximum values, $d_{1,\max}$ and $d_{2,\max}$, so that their magnitudes are comparable when calculating the norm of (20) [29].

Let J^* represent the minimum value of J obtained using the full state (i.e., unstructured) FB matrix **K** of (18); it represents the best positioning performance that can be achieved using $\mathbf{C}_{fb}$ defined in (19). The corresponding optimal CL disturbance transfer function, $\mathbf{S}_d^*$, can be expressed as

$$\mathbf{S}_d^* = -\frac{1}{D_{cl}^*}\begin{Bmatrix} s\left[\left(c-K_{24}^*\right)s+\left(k-K_{22}^*\right)\right]d_{1,\max} \\ s\left[m_1 s^2+\left(b_1+c+K_{14}^*\right)s+\left(k+K_{12}^*\right)\right]d_{2,\max}\end{Bmatrix}^{\mathrm{T}}; \quad (22)$$

$$D_{cl}^* \triangleq a_{cl,5}^* s^5 + a_{cl,4}^* s^4 + a_{cl,3}^* s^3 + a_{cl,2}^* s^2 + a_{cl,1}^* s + a_{cl,0}^*.$$

The coefficients of D^*_{cl} are functions of $K^*_{11}\ldots K^*_{25}$ and the plant parameters; their expressions are given in the Appendix. Note that the asterisk attached to the gains indicates that they are the optimal gains. A sufficient (but not necessary) condition to achieve J^*, irrespective of the type of norm or weighting function (W_e) used in (20), is to match the numerator and denominator coefficients of $\mathbf{S}_d^*$. Matching these coefficients mathematically means that the gain matrix $\mathbf{K}$, with 10 degrees of freedom (i.e., 10 gains to be determined), should satisfy 9 linear/bilinear equations; 4 for the numerators of $\mathbf{S}_d^*$ and 5 for their common denominator. Therefore, at least 1 gain in $\mathbf{K}$ is redundant.

In practice, it is not uncommon for the condition $d_{1,\max} << d_{2,\max}$ to hold. This is because d_1 is primarily the result of Coulomb friction in the bearings of the rotary motor, which is often of much smaller magnitude than the largest cutting force magnitude associated with d_2. Even when the Coulomb friction of the bearings is non-negligible, it can be measured and cancelled out reliably through feed forward friction compensation so that the FB controller does not have to deal with it. One can therefore conveniently consider $d_{1,\max} \approx 0$, such that $\mathbf{S}_d^*$ is reduced to a scalar transfer function which can be matched using 7 gains. This leaves at least 3 redundant gains to achieve J^*.

2) Use of Redundant Gains for Optimizing Efficiency

The set of all FB control inputs, $\mathbf{u}_{fb}$, that yield the same e_2 under the influence of a given disturbance input, $\mathbf{d}$, must satisfy the relationship

$$\begin{aligned} & x_2 = G_{21}\left(u_{fb1}+d_1\right)+G_{22}\left(u_{fb2}+d_2\right) \\ & \Rightarrow G_{21}\delta u_{fb1}+G_{22}\delta u_{fb2}=0. \end{aligned} \quad (23)$$

where $\delta d_1 = \delta d_2 = \delta x_2 = 0$ because they are each specified, even if unknown, functions of time. Also, the most efficient control inputs must minimize the energy functional,

$$\int\left(\left(\frac{u_{fb1}}{K_{m1}}\right)^2+\left(\frac{u_{fb2}}{K_{m2}}\right)^2\right)dt \Rightarrow \frac{u_{fb1}}{{K_{m1}}^2}\delta u_{fb1}+\frac{u_{fb2}}{{K_{m2}}^2}\delta u_{fb2}=0. \quad (24)$$

Notice that (23) and (24) are the same constraints expressed for the FF controller in (5) and (7), respectively. Combining (23) and (24) we get

$$\frac{u_{fb1}}{u_{fb2}}=\beta; \quad \beta \triangleq \kappa^2\frac{G_{21}}{G_{22}}. \quad (25)$$

The implication of (25) is that to satisfy a given e_2 requirement at maximum efficiency, the control inputs are bound by an optimal transfer function relationship given by β. This result is very powerful and can be used to directly or indirectly determine a FB controller that achieves the best performance, J^*, more efficiently than the optimal full state FB controller.

a. Energy-efficient FB Controller Design − Direct Approach

The direct approach seeks to structure $\mathbf{K}$ such that (25) is satisfied (as much as possible) without compromising J^*. To do this, note that $\mathbf{u}_{fb}$ can be written as

$$\begin{aligned} & \mathbf{u}_{fb} = \mathbf{S}_u\bar{\mathbf{d}}, \\ & \bar{\mathbf{d}} \triangleq \begin{Bmatrix}\bar{d}_1 & \bar{d}_2\end{Bmatrix}^{\mathrm{T}}, \quad \mathbf{S}_u \triangleq -\mathbf{C}_{fb}\left(\mathbf{I}+\mathbf{G}\mathbf{C}_{fb}\right)^{-1}\mathbf{G}\mathbf{W}_d, \end{aligned} \quad (26)$$

where $\bar{d}_1, \bar{d}_2 \in [-1, 1]$ represent the scaled values of d_1 and d_2, respectively. Combining (26) with (25), we get the relationship that must be satisfied by the elements of the re-structured $\mathbf{K}$ in order to maximize efficiency; it is given by

$$\begin{aligned} & u_{fb1}-\beta u_{fb2}=0 \\ & \Rightarrow \begin{cases}\Gamma_1 \triangleq \left(\mathbf{K}_1{}^{\mathrm{T}}\mathbf{Q}\mathbf{K}_2+\mathbf{p}_2{}^{\mathrm{T}}\mathbf{K}_1-\beta\mathbf{p}_2{}^{\mathrm{T}}\mathbf{K}_2\right)d_{1\max}=0 \\ \Gamma_2 \triangleq \left(\mathbf{p}_1{}^{\mathrm{T}}\mathbf{K}_1-\beta\left(\mathbf{K}_1{}^{\mathrm{T}}\mathbf{Q}\mathbf{K}_2+\mathbf{p}_1{}^{\mathrm{T}}\mathbf{K}_2\right)\right)d_{2\max}=0\end{cases} \end{aligned} \quad (27)$$

where

$$\mathbf{p}_1=\begin{bmatrix} m_1s^2+\left(c+b_1\right)s+k \\ cs^2+ks \\ m_1s^3+\left(c+b_1\right)s^2+ks \\ cs^3+ks^2 \\ m_1s^4+\left(c+b_1\right)s^3+ks^2\end{bmatrix}, \mathbf{p}_2=\begin{bmatrix} cs+k \\ m_2s^3+\left(c+b_2\right)s^2+ks \\ cs^2+ks \\ m_2s^4+\left(c+b_2\right)s^3+ks^2 \\ cs^3+ks^2\end{bmatrix}$$

$$\mathbf{Q}=\begin{bmatrix} 0 & -1 & 0 & -s & 0 \\ 1 & 0 & s & 0 & s^2 \\ 0 & -s & 0 & -s^2 & 0 \\ s & 0 & s^2 & 0 & s^3 \\ 0 & -s^2 & 0 & -s^3 & 0\end{bmatrix}, \quad (28)$$

$$\mathbf{K}_i=\begin{bmatrix}K_{i1} & K_{i2} & K_{i3} & K_{i4} & K_{i5}\end{bmatrix}^{\mathrm{T}} \quad (i=1,2).$$

Substituting $s = j\omega$ into $\Gamma_1(s)$ and $\Gamma_2(s)$ in (27) (where ω represents the frequency content of $\mathbf{d}$), we get a pair of complex-valued equations which are bilinear with respect to the elements of $\mathbf{K}$. The real and imaginary parts of both equations must equal zero at every ω contained in $\mathbf{d}$ in order to attain optimal efficiency. Obviously, $\mathbf{K}$ may not have enough redundant gains to satisfy the equations for every ω contained in $\mathbf{d}$. Therefore, one can maximize efficiency using the available redundancy by determining the $\mathbf{K}$ that minimizes the least-squares objective

$$\min J_{ee\_d} \triangleq \boldsymbol{\Gamma}(j\omega)^{\mathrm{H}}\boldsymbol{\Gamma}(j\omega) \text{ s.t. } \begin{cases}\text{stability constraints} \\ \left\|\left[W_e\mathbf{S}_d\right]\right\| = J^*\end{cases}, \quad (29)$$

where $\boldsymbol{\Gamma} = [\Gamma_1(j\omega), \Gamma_2(j\omega)]^{\mathrm{T}}$ and the superscript H represents the Hermitian transpose. If needed, the least squares objective in (29) can be weighted to emphasize some frequencies over others.

b. Energy-efficient FB Controller Design − Indirect Approach

The traditional approach for enforcing an energy efficient structure in $\mathbf{K}$ is to optimize for energy efficiency with positioning performance constraints; i.e.,

$$\min J_{ee-in} \triangleq \left\|\left[\mathbf{W}_u\mathbf{S}_u\right]\right\| \text{ s.t. } \begin{cases}\text{stability constraints} \\ \left\|\left[W_e\mathbf{S}_d\right]\right\| = J^*\end{cases}, \quad (30)$$

where $\mathbf{S}_u$ is the transfer function matrix from input $\bar{\mathbf{d}}$ to output $\mathbf{u}_{fb}$ as defined in (26), $\mathbf{W}_u$ is a diagonal weighting matrix whose elements reflect knowledge about the relative efficiencies of

the actuators. The addition of the constraint related to J^* indicates the knowledge that there is redundancy in **K** such that the same performance can be achieved in a more efficient manner. The weighting matrix, $\mathbf{W}_u$, is very important because it indirectly determines the structure of **K** used in the optimization; a poor choice of $\mathbf{W}_u$ could lead to a sub-optimal structure for **K**, which cannot attain the best energy efficiency. In practice, $\mathbf{W}_u$ is typically chosen by intuition or trial and error. However, the optimum structure for **K** can be obtained, in theory, by selecting $\mathbf{W}_u = \text{diag}([1, \beta])$, thereby eliminating the sub-optimality that could be created by a poor choice of $\mathbf{W}_u$. Notice that the setup of (30) is very similar to (29). The only difference is that the objective in (29) is designed to directly enforce (as much as possible) the optimal relationship between u_{fb1} and u_{fb2}. On the other hand, (30) enforces the optimal relationship indirectly by minimizing the feedback control forces using a suitable norm of $\mathbf{S}_u$, weighted by $\mathbf{W}_u$. A demonstration of the direct and indirect approaches is provided in Section IV.

It must be noted before leaving this section that the assumption of a static FB controller in (16) is arbitrary. It has been made purely based on its relevance to the desired control method for the HFD (which seeks to avoid high-order controllers). The methods proposed in this section can also be applied to the design of dynamic controllers (e.g., controllers with observers). Moreover, even though the proposed FF and FB controller design methods are presented in the context of the HFD described in Section II, they can be applied more broadly to other HFDs. The methods are valid as long as the plant is dual input, controllable and minimum phase with positioning performance defined on one of its outputs (e.g., x_2 in this paper).

C. Stability Constraints and Higher-order Dynamics

Thus far, only the low-order dynamics of the HFD, which is assumed to be accurately represented by its two-mass model, **G**, has been considered. Note, however, that stability constraints cannot be enforced in (20), (29) or (30) based on a CL system determined using **G**. This is because **G** has no NMP zeros, hence the gains of the FB controller can be infinitely high without causing any stability issues [29]. To enforce stability constraints, the actual plant dynamics $\mathbf{G}_a$, which includes un-modeled higher-order dynamics, must be considered. Let us assume that $\mathbf{G}_a$ is available in the form of a plant model or a frequency response function (FRF) measured at discrete frequencies, ω. Let N_p denote the number of unstable poles in the system's loop transfer function given by $\mathbf{L} = \mathbf{G}_a\mathbf{C}_{fb}$. According to the Generalized Nyquist Theorem [29], the CL system is stable if and only if the Nyquist curve of $\det(\mathbf{I} + \mathbf{L})$ makes N_p counter-clockwise encirclements of the origin without passing the origin.

Most often, it is desired to enforce robust stability, meaning that there are sufficient margins of stability. This is achieved by confining the maximum singular values $\bar{\sigma}$ of the CL sensitivity function, $\mathbf{S} = (\mathbf{I} + \mathbf{L})^{-1}$, below a specified threshold $\bar{\sigma}_{\max}$ at frequencies above the CL bandwidth, ω_{BW}, where instability is likely to occur [29]; i.e.

$$\underbrace{\bar{\sigma}\left([\mathbf{I} + \mathbf{L}(j\omega)]^{-1}\right)}_{\omega > \omega_{BW}} \le \bar{\sigma}_{\max}. \tag{31}$$

IV. Simulations and Experiments

Simulation and experiment results are presented in this section to demonstrate the effectiveness of the proposed FF and FB controller design methods. Fig. 4 shows an in-house built prototype of the HFD discussed in Section II.A. The motor constants for its rotary and linear motors are $K_{m1} = 380.8$ N/$\sqrt{\text{W}}$ and $K_{m2} = 21$ N/$\sqrt{\text{W}}$, respectively, where K_{m1} has been converted from its nominal value in Nm/$\sqrt{\text{W}}$ using a factor of $2\pi/l$, with lead $l = 5 \times 10^{-3}$ m. Therefore, $\kappa^2 = (K_{m1}/K_{m2})^2 = 328.8$, indicating two orders of magnitude difference in the efficiencies of the two actuators. The HFD is modeled as a two mass system whose parameters, reported in Table I, are identified by curve fitting measured FRFs. Fig. 5 compares the FRFs of the two-mass model (i.e., $\mathbf{G}(j\omega)$) with the experimentally measured FRFs (i.e., $\mathbf{G}_a(j\omega)$). As seen, the two FRFs are in good agreement up to 100 Hz, hence **G** captures the critical axial/torsional mode of the HFD, occurring at 41 Hz.

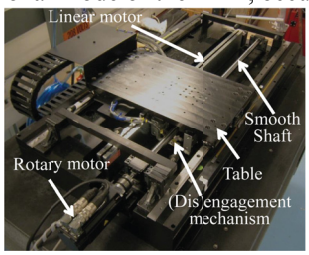

Fig. 4. HFD Prototype used for Simulations and Experiments

TABLE I
IDENTIFIED PARAMETERS OF THE HFD'S TWO-MASS MODEL

m_1 [kg]	616.2	b_1 [kg/s]	44.8	c [kg/s]	5777.2
m_2 [kg]	46.3	b_2 [kg/s]	83.3	k [N/μm]	3.1469

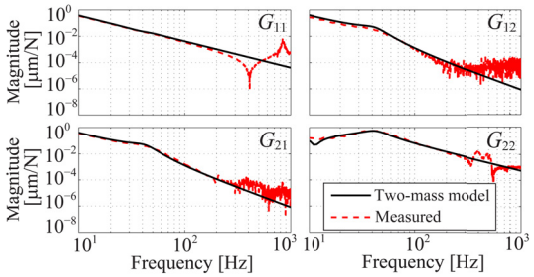

Fig. 5. Comparison of Two-mass Model with Experimentally Measured FRF

A. Evaluation of FF Controllers using Simulations

Simulations are conducted to evaluate the tracking performance and energy efficiency of the near energy optimal (NEO) FF control method proposed in Section III.A. FB control is not considered in the simulations because the plant is assumed to be perfectly described by its two-mass model, **G**, and no disturbances are introduced. Under the conditions described, the proposed NEO FF controller is able to achieve perfect tracking with near optimal or optimal efficiency, depending on whether G_{ff} defined in (8) has NMP zeros or not. Evaluating G_{ff} using the reported parameters of the HFD reveals that it has a complex conjugate pair of NMP zeros located at $s = 196 \pm 314j$. Therefore, the gain K_{ff} must be

selected to ensure a stable inverse of G_{ff-neo} while providing near energy optimality. Fig. 6 shows the root locus of G^{-1}_{ff-neo} as K_{ff} is varied in the interval $[0, \infty)$. It is found that the unstable pole pair in G^{-1}_{ff-neo} (corresponding to the NMP zero pair in G_{ff-neo}) becomes stable for values of $K_{ff} \geq 30.3$. Note that the point marked $K_{ff} = 1000$ has been highlighted on purpose in the figure; it represents a value of K_{ff} which is utilized for comparative simulations later in this section.

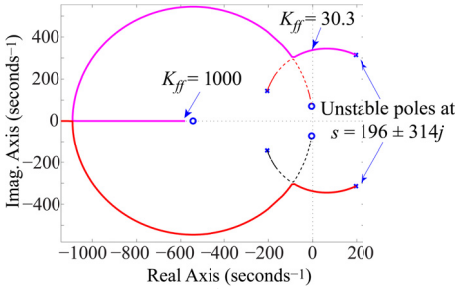

Fig. 6. Root Locus of G^{-1}_{ff-neo} as a Function of K_{ff}

For tracking tests, a desired position trajectory, x_d, of stroke 15 mm, with kinematic limits of 100 mm/s, 1×10^4 mm/s^2, 1.5×10^6 mm/s^3 and 5×10^8 mm/s^4 for velocity, acceleration, jerk and snap, respectively, is used. Its velocity profile is shown in Fig. 7(a); its position, acceleration, jerk and snap profiles are omitted due to space limitations. A FF technique called rigid body FF (RB FF) [42] is used as the benchmark for evaluating the proposed NEO FF controller. RB FF is generated by specifying $x_{r1} = x_{r2} = x_d$ such that

$$\mathbf{u}_{ff} = \mathbf{G}^{-1}\begin{Bmatrix} x_d & x_d \end{Bmatrix}^{\mathrm{T}} = \begin{Bmatrix} m_1 s^2 + b_1 s \\ m_2 s^2 + b_2 s \end{Bmatrix} x_d. \tag{32}$$

The implication of (32) is that in RB FF each actuator is given the responsibility to move the mass to which it is attached, such that the two-mass system moves as one rigid body. It is very elegant and it guarantees perfect tracking. Note that the zero phase error FF approximation of (10) is not selected as the benchmark because it does not meet the perfect tracking requirement stipulated for FF control.

Fig. 7 (b)-(d) and Table II compare the tracking error (e_2) at the table, and the power/heat wasted by each actuator using RB FF and the proposed NEO FF, with $K_{ff} = 30.3$ and $K_{ff} = 1000$. All three controllers achieve perfect tracking, as expected. Notice, however, that RB FF depends heavily on the inefficient LMD. As a result, it is 71.5% less efficient than NEO FF, using $K_{ff} = 1000$. In theory, NEO FF with $K_{ff} = 30.3$ should be the most efficient. However, notice from the figure that $K_{ff} = 30.3$ results in undesirable ringing of the control signals because it gives rise to poorly damped poles in G^{-1}_{ff-neo}. The near optimal energy formulation of (12) does not recognize the effect of poorly damped poles/zeros (much like the optimal energy formulation of (8) misses the effect of NMP poles/zeros). Therefore, the onus falls on the controller designer to select a value of K_{ff} that is high enough to avoid poorly damped poles in G^{-1}_{ff-neo}. Fig. 8 plots the total heat energy of NEO FF in tracking the reference trajectory of Fig. 7(a) using values of K_{ff} ranging from 30.3 to 1000. Notice that the energy is initially very high but drops rapidly as the value of K_{ff} increases and the poles become more damped. For this particular case, the energy continues to reduce as K_{ff} is increased but the rate of decrease becomes very low after about $K_{ff} = 50$. The decrease in energy continues until $K_{ff} = 1000$ and beyond, but the difference between the energy at $K_{ff} = 1000$ and that at $K_{ff} = 10{,}000$ is just 0.03 J. It must be noted that the relationship between K_{ff} and energy highly depends on the system and desired trajectory. (For instance see the Appendix for the energy vs. K_{ff} plot of a slightly different desired trajectory). Nonetheless, it appears that as long as K_{ff} is tuned to provide sufficiently damped poles in G^{-1}_{ff-neo}, the energy performance remains near optimal.

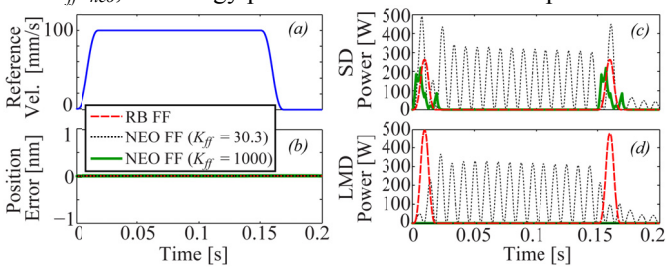

Fig. 7. Reference Velocity Profile and Comparison of Tracking Errors and Actuator Power of FF Controllers (Simulation)

TABLE II
COMPARISON OF TRACKING ERRORS AND ENERGY EFFICIENCY OF FF CONTROLLERS BASED ON SIMULATION RESULTS

	RB FF	NEO FF (K_{ff} = 30.3)	NEO FF (K_{ff} = 1000)
Max Tracking Error [nm]	0.000	0.000	0.000
Heat Energy SD [J]	3.967	27.918	3.242
Heat Energy LMD [J]	7.398	24.358	0.001
Total Heat Energy [J]	11.365	52.276	3.243

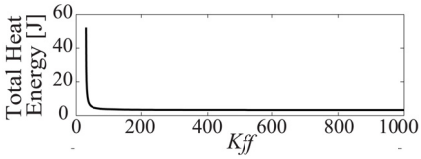

Fig. 8. Total Heat Energy of Proposed NEO FF as a Function of K_{ff} (based on Reference Trajectory of Fig. 7(a)) – Simulation

B. Evaluation of FB Controllers using Simulations

Simulations are conducted to evaluate EE direct and EE indirect, the direct and indirect methods for using the optimal transfer function relationship, β, derived in Section III.B for FB controller design. The benchmark is selected as the full (i.e., unstructured) state FB controller discussed in Section III.B. The practical scenario where $d_{1,\max} = 0$ and $d_{2,\max} = 400$ N (which is the cutting force limit of the HFD of Fig. 4 [27]) is assumed. MATLAB's *hinfstruct* command (which performs H_∞ optimization based on a structured gain matrix) is used to determine the $\mathbf{S}_d^*$ that minimizes the objective of (20) using the H_∞ norm. A weighting function, W_e, suggested by Skogestad and Postlethwaite [29] is adopted; it is given by

$$W_e = \frac{\left(s/M^{1/n} + \omega_B\right)^n}{\left(s + \omega_B A^{1/n}\right)^n}, \tag{33}$$

Equation (33) represents a filter of order n, designed to weight very low frequencies by a factor of M/A compared to very high frequencies (i.e., frequencies much higher than ω_B), so as to enforce integral action. We select $n = 2$, $M = 2$, $A = 5 \times 10^{-6}$ and

$\omega_B = 200\pi$ rad/s (indicating that we want integral action to taper off beyond 100 Hz).

The HFD is assumed to be perfectly modeled by **G**, and the table-side disturbance force, d_2, is assumed to be a harmonic cutting force at 60 Hz, with an additional DC component; it is given by

$$d_2(t) = 200 + 200\sin(120\pi t) \text{ [N]}. \quad (34)$$

However, as discussed in Section III.C, applying the optimization of (20) to **G** could yield infinitely large gains. Therefore, a 7th order Butterworth low-pass filter, with cutoff frequency of 1000 Hz, is applied to each element of **G** before carrying out the H_∞ optimization in order to have finite stability limits. The default stability settings of MATLAB's *hinfstruct* command are maintained for the optimization. The resulting $\mathbf{S}_d^*(1,2)$ (scaled by $1/d_{2,\max}$) is plotted in Fig. 9(a) and the elements of the optimal full state FB gain matrix (i.e., $\mathbf{K}^*$) are given in Table III. Note that only $\mathbf{S}_d^*(1,2)$ is shown in the figure because $\mathbf{S}_d(1,1) = 0$ based on the assumption that $d_{1,\max} = 0$.

Fig. 9(b) shows the optimal transfer function relationship, β, for the HFD. It requires the magnitude of the ratio u_{fb1}/u_{fb2} to be 50.3 dB at $\omega = 0$, and to be 23.5 dB at $\omega = 120\pi$ rad/s. In employing β for energy efficiency optimization of **K**, we have chosen to use $\mathbf{S}_d^*$ instead of its infinity norm, J^*, as the performance constraint in (29) and (30). This is done in order to ensure that the exact same regulation performance as the optimal full state FB controller is achieved at all frequencies. Therefore, using (22), we derive 7 constraint equations to ensure that the poles and zeros of $\mathbf{S}_d^*(1,2)$ are matched with 7 out of the 10 gains of **K**, leaving us with 3 redundant gains. To obtain the energy efficient controller using the direct method (i.e., EE direct), one of the remaining 3 gains is used to perfectly enforce (27) at $\omega = 0$. In theory, the last two gains could be used to satisfy the real and imaginary parts of (27) at $\omega = 120\pi$ rad/s, but the equations are highly nonlinear and difficult to solve analytically. Therefore, the remaining two gains are used to minimize $J_{ee\text{-}d}$ (i.e., (29)) at $\omega = 120\pi$ rad/s. The elements of the resulting gain matrix are given in Table III.

To determine the energy efficient controller using the indirect method (i.e., EE indirect), MATLAB's *hinfstruct* command is used to minimize the H_∞ norm of (30). A weighting function given by $\mathbf{W}_u = W_\omega \text{diag}([1, \beta])$ is selected, where W_ω is a weighting filter designed to emphasize frequencies $\omega = 0$ and $\omega = 120\pi$ rad/s contained in d_2. It is defined as

$$W_\omega = W_e \frac{\omega_n^2}{s^2 + 2\zeta\omega_n s + \omega_n^2}, \quad (35)$$

Note that W_e is the exact same filter defined in (33); it is used in W_ω to place a higher weight on frequencies close to $\omega = 0$. The second-order filter multiplying W_e is designed with $\omega_n = 120\pi$ rad/s and $\zeta = 8.2\times10^{-6}$, such that its magnitude at resonance is equal to $W_e(0)$. The constraint equations that were used to match the poles and zeros of $\mathbf{S}_d^*(1,2)$ for the EE direct method are used to structure **K** within MATLAB's *hinfstruct* function so that $\mathbf{S}_d^*(1,2)$ is also matched perfectly in EE indirect. The elements of the resulting FB gain matrix are reported in Table III.

Fig. 9(a) compares the magnitudes of $\mathbf{S}_d(1,2)/d_{2,\max}$ for the EE direct and EE indirect controllers to the original $\mathbf{S}_d^*(1,2)/d_{2,\max}$ determined based on the optimal state FB controller; the plots are coincident, indicating that all three methods achieve the best positioning performance at all frequencies. Fig. 9 (c) and (d) respectively compare $\mathbf{S}_u(1,2)/d_{2,\max}$ and $\mathbf{S}_u(2,2)/d_{2,\max}$ for the three methods. Notice that $\mathbf{S}_u(1,2)/\mathbf{S}_u(2,2) = 50.3$ dB for the EE direct controller, meaning that it perfectly matches β at $\omega = 0$. However, at $\omega = 120\pi$ rad/s, it achieves a $\mathbf{S}_u(1,2)/\mathbf{S}_u(2,2)$ ratio of 32 dB instead of the 23.5 dB stipulated by β, due to errors in the least squares solution applied at that frequency. The EE indirect controller does not perform as well as the EE direct in terms of matching β. This is because, in determining the gain matrix for the EE indirect controller, the *hinfstruct* command was initialized with the gain matrix of the optimal full state FB controller (i.e., $\mathbf{K}^*$). Comparing the elements of the full state FB controller's gain matrix to those of the EE indirect controller in Table III, one can conclude that the gradient-based algorithm used in *hinfstruct* may have gotten stuck in a local minimum close to its initial value, thus preventing it from reaching a better solution. This is a well-known limitation of gradient based methods when performing non-convex optimizations. It could be mitigated by testing various initial values in hopes of finding other local minima. Note that the direct method was also initialized with the elements of the full state FB matrix, when performing the nonlinear least-squares optimization of (29). Therefore, its solution could also get stuck in local minima around its starting point, but it appears from Table III that its gains are quite different from those of the full state FB matrix.

The expression

$$\sum_{i=1}^{2} \frac{1}{K_{mi}^2} \left\{ \left(200 \left| \frac{\mathbf{S}_u^T(2,i)}{d_{2,\max}} \right|_{\omega=0} \right)^2 + \frac{1}{2} \left(200 \left| \frac{\mathbf{S}_u^T(2,i)}{d_{2,\max}} \right|_{\omega=120\pi} \right)^2 \right\}, \quad (36)$$

representing the sum of the average power at $\omega = 0$ and $\omega = 120\pi$ rad/s of each actuator's steady-state response to $d_2(t)$ given in (34), is used to calculate the average power dissipated in heat by each FB controller. The results are shown in Table IV. EE direct and EE indirect are respectively 60% and 33% more efficient than the full state FB method. Fig. 10 compares the ratio of the average power of the EE direct and EE indirect based controllers, relative to that of the full state FB controller, using a disturbance input of $d_2(t) = \sin(2\pi f t)$. The EE direct controller is much more efficient than the full controller from $f = 0$ through $f = 44$ Hz, after which it becomes less efficient. Note that its relative efficiency is 8 dB worse at $f = 60$ Hz, due to the aforementioned errors in the least square solution. The EE indirect controller, on the other hand, is more efficient than the full controller at all frequencies, but only by a very small (0.6 dB) margin (except at $f = 0$ and $f = 60$ Hz where it shows slightly better relative efficiencies of 4.2 dB and 0.8 dB, respectively).

TABLE III
COMPARISON OF ELEMENTS OF FB GAIN MATRICES CALCULATED USING THE FULL STATE FB, EE DIRECT AND EE INDIRECT METHODS (SIMULATION)

	K_{11}	K_{12}	K_{13}	K_{14}	K_{15}
Full State FB	-8.2×10^{5}	-3.1×10^{6}	-3.1×10^{8}	-5.8×10^{3}	-9.3×10^{5}
EE direct	$+9.2\times10^{5}$	-3.1×10^{6}	$+3.8\times10^{9}$	-5.8×10^{3}	$+8.5\times10^{6}$
EE indirect	-4.5×10^{5}	-3.1×10^{6}	-1.8×10^{8}	-5.8×10^{3}	-6.2×10^{5}
	K_{21}	K_{22}	K_{23}	K_{24}	K_{25}
Full State FB	-2.4×10^{10}	$+4.2\times10^{7}$	$+5.2\times10^{7}$	$+9.5\times10^{4}$	$+1.6\times10^{5}$
EE direct	-5.2×10^{7}	-7.6×10^{4}	$+1.1\times10^{8}$	-8.9×10^{1}	$+1.6\times10^{5}$
EE indirect	-2.3×10^{10}	$+7.0\times10^{7}$	$+6.8\times10^{7}$	$+1.3\times10^{5}$	$+1.6\times10^{5}$

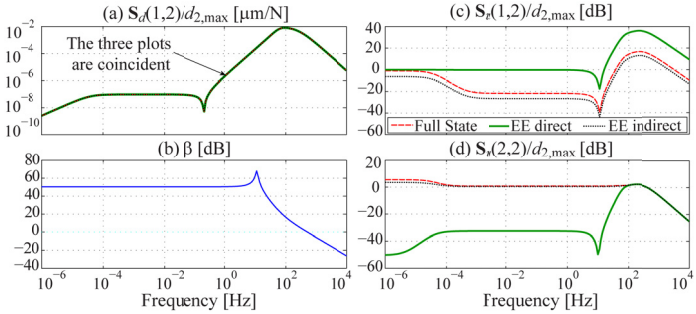

Fig. 9. Comparison of Positioning Performance and Control Effort of the Full State FB and the Energy-efficient FB Controllers designed using the EE Direct and EE Indirect Approaches (Simulation)

TABLE IV
COMPARISON OF ENERGY EFFICIENCY OF FB CONTROLLERS BASED ON EQUATION (36) (SIMULATION)

Average Power Dissipated in Heat	Full State FB	EE direct	EE indirect
SD [W]	1.36	125.80	0.51
LMD [W]	381.80	26.31	254.44
Total [W]	383.16	152.11	254.95

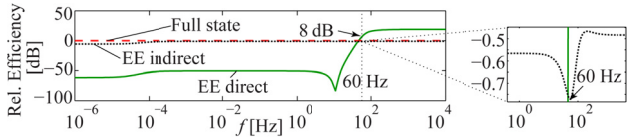

Fig. 10. Comparison of Efficiencies of Controllers designed using the EE Direct and EE Indirect Methods (Relative to Efficiency of Full State FB Controller) – Simulation

C. Machining Experiments

Machining experiments are conducted to evaluate the performance and energy efficiency of the proposed controller design methods. To perform the experiments, the HFD prototype of Fig. 4 is mounted on the x axis of a FADAL VMC 4020 3-axis milling machine to cut a 15 mm long, 1 mm deep slot in an AISI 1018 steel workpiece. Table V summarizes the key cutting parameters for the operation. A spindle speed of 3600 rpm (i.e., 60 Hz) is selected for the cutting tests. To maintain a reasonable feed per tooth, the desired position trajectory, x_d, is prescribed to travel at a maximum speed of 300 mm/min (i.e., 5 mm/s), with acceleration, jerk and snap limits of 62.5 mm/s^2, 3125 mm/s^3 and 6.25×10^5 mm/s^4, respectively. At such low speeds and accelerations, the theoretical energy contributions of RB FF and NEO FF are negligible (< 6 mJ), and are indistinguishable from noise in the control signals. Consequently, the effect of FF is not considered in the machining tests.

TABLE V
CUTTING PARAMETERS

Spindle speed	3600 rpm
Tool	3/8" dia. HSS end mill
Number of flutes	4
Feed per tooth	0.02 mm/tooth
Feed rate	300 mm/min
Lubrication	None

The optimal full state FB controller is designed by optimizing the H_∞ norm of (20) with the actual (i.e., measured) plant dynamics, $\mathbf{G}_a(j\omega)$, substituted for $\mathbf{G}$. The Coulomb friction in the bearings of the rotary motor is small and can be easily cancelled by feed forward action. Therefore, $d_{1,\max} = 0$ is assumed, and $d_{2,\max}$ is selected as 400 N. Notch filters are placed at the 847 Hz resonance peak appearing in $\mathbf{G}_a(1,1)$ (in Fig. 5), and at the 400 Hz and 487 Hz resonance peaks appearing in $\mathbf{G}_a(2,2)$ in order to increase stability margins. Robust stability constraints are enforced by limiting the maximum singular values of the sensitivity function for frequencies higher than ω_{BW} = 628 rad/s (100 Hz) to $\bar{\sigma}_{\max} = 2.65$.

MATLAB's *hinfstruct* command, which was used in the simulations, could not be employed for carrying out the optimization in (20) using $\mathbf{G}_a$ instead of $\mathbf{G}$. This is because $\mathbf{G}_a$ is given as a FRF at discrete frequencies, not as a transfer function modeled in s-domain. Therefore, a Particle Swarm Optimization (PSO) Toolbox in MATLAB [43] is used to carry out the H_∞ optimization, based on a technique similar to the one reported in [44]. The elements of the resulting optimal full state FB gain matrix are provided in Table VI.

Feed forces in milling typically have a DC portion, as well as harmonics at the spindle and tooth passing frequencies [45]. Therefore, for the EE direct controller, we follow the exact same procedure as used in Section IV.B. The elements of $\mathbf{K}$ are constrained to match $\mathbf{S}_d^*(1,2)$ using (22), and the 3 redundant gains are used for enforcing the β constraint at $\omega = 0$ and $\omega = 120\pi$ rad/s, representing the lowest harmonic in d_2. For the EE indirect method, MATLAB's PSO toolbox is used to carry out the optimization of (30) based on $\mathbf{G}_a$, with the elements of $\mathbf{K}^*$ as its initial values; constraints are added to match $\mathbf{S}_d^*(1,2)$ using (22), following the exact same procedure as in the simulations reported in Section IV.B. The gains of the EE direct and indirect controllers are reported in Table VI.

TABLE VI
COMPARISON OF ELEMENTS OF FB GAIN MATRICES CALCULATED USING THE FULL STATE FB, EE DIRECT AND EE INDIRECT METHODS (EXPERIMENTS)

	K_{11}	K_{12}	K_{13}	K_{14}	K_{15}
Full State FB	4.65×10^{7}	4.92×10^{5}	1.06×10^{8}	1.29×10^{4}	6.50×10^{5}
EE Direct	5.48×10^{7}	4.92×10^{5}	8.90×10^{7}	1.29×10^{4}	5.93×10^{5}
EE Indirect	4.80×10^{7}	4.92×10^{5}	8.57×10^{7}	1.29×10^{4}	5.46×10^{5}
	K_{21}	K_{22}	K_{23}	K_{24}	K_{25}
Full State FB	1.52×10^{7}	6.15×10^{5}	1.02×10^{7}	4.85×10^{2}	4.30×10^{4}
EE Direct	2.54×10^{6}	1.59×10^{5}	1.12×10^{7}	1.02×10^{3}	4.30×10^{4}
EE Indirect	6.16×10^{6}	1.57×10^{4}	1.06×10^{7}	-4.25×10^{1}	4.30×10^{4}

Fig. 11(a) compares $\mathbf{S}_d(1,2)/d_{2,\max}$ generated using the EE direct and EE indirect controllers to $\mathbf{S}_d^*(1,2)/d_{2,\max}$, generated using the full state FB controller. An almost perfect match is

obtained, indicating that the positioning performances of all three controllers are virtually the same. Fig. 11(b) compares the maximum singular values of the CL sensitivity function for the three controllers; they are very similar and all satisfy $\bar{\sigma}_{\max} \leq 2.65$ for frequencies above 100 Hz. Fig. 11 (c) and (d) respectively compare $\mathbf{S}_u(1,2)/d_{2,\max}$ and $\mathbf{S}_u(2,2)/d_{2,\max}$ of all three controllers. In both figures, the two-mass model, $\mathbf{G}$, has been used to generate data below 10 Hz which are not contained in the measured FRF, $\mathbf{G}_a$. Again, EE direct is able to match the β criterion at $\omega = 0$. At $\omega = 120\pi$ rad/s, $\mathbf{S}_u(1,2)/\mathbf{S}_u(2,2) = 21.7$ dB, which is much closer to the target value of 23.5 dB than obtained in the simulations. A plot of the efficiencies of the EE direct and indirect controllers is provided in Fig. 12, following the same procedure used in the simulation to generate Fig. 10. The EE direct controller is more efficient than the full state FB controller for frequencies ranging from $f = 0$ to $f = 170$ Hz; and at its worst, it is only 0.3 dB less efficient than the full state FB controller (at 848 Hz). The EE indirect controller is 3.1 dB and 2.8 dB more efficient than the full state FB controller at $f = 0$ and $f = 60$ Hz, respectively; at its worst, it is 3.8 dB less efficient than the full state FB controller (at 0.83 Hz).

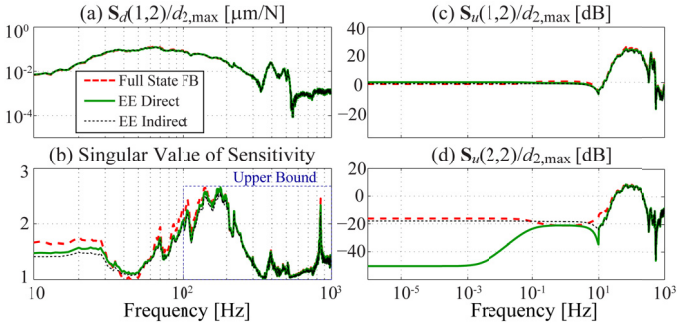

Fig. 11. Comparison of Positioning Performance, Robustness and Control Effort of the Full State FB and the Energy-efficient FB Controllers designed using the EE Direct Approach based on Experiments

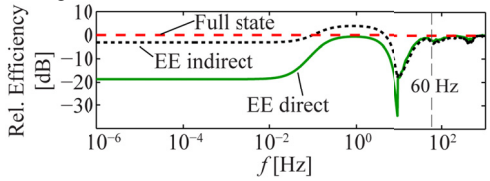

Fig. 12. Comparison of Efficiencies of Controllers designed using the EE Direct and EE Indirect Methods (Relative to Efficiency of Full State FB Controller) – Experiments

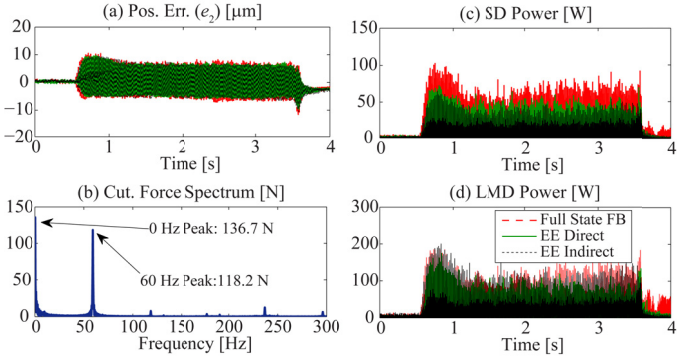

Fig. 13. Plots of Positioning Error, Cutting Force Spectrum and Actuator Power Dissipated in Heat during Machining Experiment

The controllers are implemented on a dSPACE 1103 motion control platform at a sampling frequency of 10 kHz. A table-mounted high-resolution encoder (see Fig. 1) is used to measure the position of the table, x_2. However, the rotary position of the motor shaft x_1 is obtained using the observer proposed in [46]. This is because readings from the motor-mounted rotary encoder had an undesirable drift caused by micro slippage, which is known to occur between the Roh'lix nut and smooth shaft [32]. The velocity feedback signals, $\dot{x}_1$ and $\dot{x}_2$, are acquired by taking discrete derivatives of the position signals measured from the rotary and linear encoders, respectively. Fig. 13 (a) shows a comparison of the positioning errors (e_2), measured from the linear encoder. Notice that all three controllers have nearly identical positioning performance, as also confirmed by the maximum and RMS errors reported in Table VII. The disturbance force d_2 during cutting is estimated from the linear motor's current by performing the cut using the LMD only (i.e., by disengaging the Roh'lix nut from the shaft). Fig. 13 (b) shows the frequency spectrum of the estimated d_2, which clearly shows dominant peaks at 0 and 60 Hz. Fig. 13 (c) and (d) show the power dissipated as heat in the SD and LMD (calculated using (4) without the integral) for each controller; Table VII summarizes the average power dissipated in heat by each actuator during cutting. Observe that even though the positioning performance of all three controllers is almost the same, the EE direct and EE indirect controllers are respectively 26% and 20% more efficient than the full state FB controller.

TABLE VII
COMPARISON OF TRACKING ERRORS AND ENERGY EFFICIENCIES OF FB CONTROLLERS BASED ON MACHINING EXPERIMENTS

	Max e_2 [μm]	RMS e_2 [μm]	SD Avg. Pwr. [W]	LMD Avg. Pwr. [W]	Total Avg. Pwr. [W]
Full State FB	12.7	4.3	13.3	24.2	37.5
EE Direct	9.7	3.8	8.8	18.9	27.7
EE Indirect	10.6	4.0	7.9	22.1	30.0

V. CONCLUSION AND FUTURE WORK

This paper has presented a method for designing a controller that achieves the best positioning performance while maximizing the energy efficiency of a redundantly-actuated hybrid feed drive (HFD). The control structure is assumed to have a feed forward (FF) controller for tracking and a feedback (FB) controller for regulation. An approach for designing the FF controller to achieve perfect tracking while remaining stable and near energy optimal has been proposed and verified using comparative simulations. For FB controller design, an optimal transfer function relationship between the control inputs of the HFD has been derived; the relationship ensures that maximum efficiency is attained for any specified performance. Two approaches have been proposed for using the derived optimal transfer function relationship for energy efficient controller design, without sacrificing performance. The first approach directly constrains the control inputs to achieve the requirements of the optimal transfer function relationship. The second approach indirectly implements the optimal relationship in the form of a weighting filter for use in traditional H_2/H_∞ controller synthesis. Simulations and machining experiments

have been used to demonstrate the benefits of the proposed approaches in significantly improving energy efficiency without sacrificing positioning performance for a redundantly-actuated HFD. The proposed FF and FB controller design methods are general enough to apply to any plant (HFD) that is dual input, controllable and minimum phase with positioning performance defined on one of its outputs. Future work will seek to generalize the proposed methods to plants with more than two inputs. Performance and stability issues that could arise when the HFD studied in this paper switches rapidly between its two modes of operation will also be investigated.

REFERENCES

[1] Y. Altintas, A. Verl, C. Brecher, L. Uriarte, and G. Pritschow, "Machine tool feed drives," *CIRP Ann. - Manuf. Technol.*, vol. 60, no. 2, pp. 779–796, 2011

[2] R. Saidur, "A review on electrical motors energy use and energy savings," *Renew. Sustain. Energy Rev.*, vol. 14, no. 3, pp. 877–898, 2010.

[3] A. Vijayaraghavan and D. Dornfeld, "Automated energy monitoring of machine tools," *CIRP Ann. - Manuf. Technol.*, vol. 59, no. 1, pp. 21–24, 2010.

[4] A. E. K. Mohammad A. M., N. Uchiyama, and S. Sano, "Energy Saving in Feed Drive Systems Using Sliding-Mode-Based Contouring Control With a Nonlinear Sliding Surface," *IEEE/ASME Trans. Mechatronics*, vol. 20, no. 2, pp. 572–579, 2015.

[5] Y. Halevi, E. Carpanzano, G. Montalbano, and G. Halevi, "Minimum Energy Control of Redundant Linear Manipulators," *J. Dyn. Syst. Meas. Control*, vol. 136, no. 5, pp. 1–8, 2014.

[6] M. S. Huang, Y. L. Hsu, and R. F. Fung, "Minimum-energy point-to-point trajectory planning for a motor-toggle servomechanism," *IEEE/ASME Trans. Mechatronics*, vol. 17, no. 2, pp. 337–344, 2012.

[7] D. Yoon and C. E. Okwudire, "Magnet assisted stage for vibration and heat reduction in wafer scanning," *CIRP Ann. - Manuf. Technol.*, vol. 64, no. 1, pp. 381–384, 2015.

[8] J. Park, "Motion profile planning of repetitive point-to-point control for maximum energy conversion efficiency under acceleration conditions," *Mechatronics*, vol. 6, no. 6, pp. 649–663, 1996.

[9] Y. Wang, Y. Zhao, K. S. Bortoff, and K. Ueda, "A Real-Time Energy-Optimal Trajectory Generation Method for a Servomotor," *IEEE Trans. Ind. Electron.*, vol. 62, no. 2, pp. 1175–1188, 2015.

[10] Y. Wang, K. Ueda, and S. A. Bortoff, "A Hamiltonian approach to compute an energy efficient trajectory for a servomotor system," *Automatica*, vol. 49, no. 12, pp. 3550–3561, 2013.

[11] M. Helu, B. Behmann, H. Meier, D. Dornfeld, G. Lanza, and V. Schulze, "Impact of green machining strategies on achieved surface quality," *CIRP Ann. - Manuf. Technol.*, vol. 61, no. 1, pp. 55–58, 2012.

[12] J. B. Dahmus and T. G. Gutowski, "An Environmental Analysis of Machining," in *Manufacturing Engineering and Materials Handling Engineering*, 2004, vol. 2004, pp. 643–652

[13] G. Pritschow and W. Philipp, "Direct Drives for High-Dynamic Machine Tool Axes," *CIRP Ann. - Manuf. Technol.*, vol. 39, no. 1, pp. 413–416, Jan. 1990

[14] A. Robert, "Attack of the linear motors," *Manuf. Eng*., vol. 5, pp. 60–64, 1997.

[15] G. Pritschow, "A Comparison of Linear and Conventional Electromechanical Dives," *CIRP Ann. - Manuf. Technol.*, vol. 47, no. 2, pp. 541–548, 1998

[16] L. Xu and B. Yao, "Adaptive robust precision motion control of linear motors with negligible electrical dynamics: theory and experiments," *IEEE/ASME Trans. Mechatronics*, vol. 6, no. 4, pp. 444–452, 2001.

[17] M. Butcher and A. Karimi, "Linear Parameter-Varying Iterative Learning Control With Application to a Linear Motor System," *IEEE/ASME Trans. Mechatronics*, vol. 15, no. 3, pp. 412–420, 2010

[18] K. Sato, M. Katori, and A. Shimokohbe, "Ultrahigh-Acceleration Moving-Permanent-Magnet Linear Synchronous Motor With a Long Working Range," *IEEE/ASME Trans. Mechatronics*, vol. 18, no. 1, pp. 307–315, 2013

[19] R. Glöß, "Nanometer precise hybrid actuator in positioning mechanism with long travel range," in *International Conference and Exhibition on New Actuators and Drive Systems, Bremen, Germany*, 2006, pp. 668–671

[20] H. J. Pahk, D. S. Lee, and J. H. Park, "Ultra precision positioning system for servo motor–piezo actuator using the dual servo loop and digital filter implementation," *Int. J. Mach. Tools Manuf.*, vol. 41, no. 1, pp. 51–63, 2001

[21] T. Fujita, A. Matsubara, D. Kono, and I. Yamaji, "Dynamic characteristics and dual control of a ball screw drive with integrated piezoelectric actuator," *Precis. Eng.*, vol. 34, no. 1, pp. 34–42, 2010

[22] L. Juhász and J. Maas, "Control of hybrid nanopositioning systems for trajectory-tracking applications," *Mechatronics*, vol. 23, no. 6, pp. 617–629, 2013

[23] S. J. Schroeck, W. C. Messner, and R. J. McNab, "On compensator design for linear time-invariant dual-input single-output systems," *IEEE/ASME Trans. Mechatronics*, vol. 6, no. 1, pp. 50–57, Mar. 2001

[24] J. Zheng, W. Su, and M. Fu, "Dual-Stage Actuator Control Design Using a Doubly Coprime Factorization Approach," *IEEE/ASME Trans. Mechatronics*, vol. 15, no. 3, pp. 339–348, 2010.

[25] H. Shinno, H. Yoshioka, and M. Hayashi, "A high performance tilting platform driven by hybrid actuator," *CIRP Ann. - Manuf. Technol.*, vol. 58, no. 1, pp. 363–366, 2009.

[26] S. Frey, K. Groh, and A. Verl, "Semi-active damping of drive systems," *J. Vib. Control*, vol. 19, no. 5, pp. 742–754, 2012

[27] C. Okwudire and J. Rodgers, "Design and control of a novel hybrid feed drive for high performance and energy efficient machining," *CIRP Ann. - Manuf. Technol.*, vol. 62, no. 1, pp. 391–394, 2013

[28] S. Kale, N. Dancholvichit, and C. Okwudire, "Comparative LCA of a Linear Motor and Hybrid Feed Drive under High Cutting Loads," *Procedia CIRP*, vol. 14, pp. 552–557, 2014

[29] S. Skogestad and I. Postlethwaite, *Multivariable feedback control: analysis and design*. Wiley New York, 2007

[30] P. Van den Braembussche, J. Swevers, and H. Van Brussel, "Design and experimental validation of robust controllers for machine tool drives with linear motor," *Mechatronics*, vol. 11, no. 5, pp. 545–562, 2001

[31] "Roh'Lix® Linear Actuators." [Online]. Available: http://www.zero-max.com/linear-motion-control-c-24-l-en.html

[32] E. S. Buice, D. Otten, R. H. Yang, S. T. Smith, R. J. Hocken, and D. L. Trumper, "Design evaluation of a single-axis precision controlled positioning stage," *Precis. Eng.*, vol. 33, no. 4, pp. 418–424, 2009

[33] K. Varanasi and S. Nayfeh, "The dynamics of lead-screw drives: low-order modeling and experiments," *J. Dyn. Syst. Meas. Control*, vol. 126, pp. 388–396, 2004

[34] C. Okwudire and Y. Altintas, "Minimum Tracking Error Control of Flexible Ball Screw Drives Using a Discrete-Time Sliding Mode Controller," *J. Dyn. Syst. Meas. Control*, vol. 131, no. 5, p. 051006, 2009

[35] D. J. Gordon and K. Erkorkmaz, "Accurate control of ball screw drives using pole-placement vibration damping and a novel trajectory prefilter," *Precis. Eng.*, vol. 37, no. 2, pp. 308–322, 2013

[36] D. Sepasi, R. Nagamune, and F. Sassani, "Tracking Control of Flexible Ball Screw Drives With Runout Effect and Mass Variation," *IEEE Trans. Ind. Electron.*, vol. 59, no. 2, pp. 1248–1256, 2012

[37] C. E. Okwudire and Y. Altintas, "Hybrid Modeling of Ball Screw Drives With Coupled Axial, Torsional, and Lateral Dynamics," *J. Mech. Des.*, vol. 131, no. 7, p. 071002, 2009

[38] D. Kirk, *Optimal control theory: an introduction*. Courier Corporation, 2012, pp. 237–240

[39] M. Tomizuka, "Zero Phase Error Tracking Algorithm for Digital Control," *J. Dyn. Syst. Meas. Control*, vol. 109, no. 1, p. 65-68, 1987

[40] B. P. Rigney, L. Y. Pao, and D. A. Lawrence, "Nonminimum Phase Dynamic Inversion for Settle Time Applications," *IEEE Trans. Control Syst. Technol.*, vol. 17, no. 5, pp. 989–1005, 2009.

[41] J. A. Butterworth, L. Y. Pao, and D. Y. Abramovitch, "Analysis and comparison of three discrete-time feedforward model-inverse control techniques for nonminimum-phase systems," *Mechatronics*, vol. 22, no. 5, pp. 577–587, 2012.

[42] M. Duan and C. Okwudire, "Energy Efficiency and Performance Optimized Control of a Hybrid Feed Drive," in *ASME 2015 International Manufacturing Science and Engineering Conference*, 2015.

[43] S. Chen, "Another Particle Swarm Toolbox," *MATLAB Central File Exchange*, 2014. [Online]. Available: http://www.mathworks.com/matlabcentral/fileexchange/25986-another-particle-swarm-toolbox/content/psopt/pso.m.

[44] T. H. Kim, I. Maruta, and T. Sugie, "Robust PID controller tuning based on the constrained particle swarm optimization," *Automatica*, vol. 44, no. 4, pp. 1104–1110, 2008.
[45] Y. Altintas, *Manufacturing automation: metal cutting mechanics, machine tool vibrations, and CNC design*. Cambridge university press, 2012.
[46] M. Darouach, M. Zasadzinski, and S. J. Xu, "Full-order observers for linear systems with unknown inputs," *IEEE Trans. Automat. Contr.*, vol. 39, no. 3, pp. 606–609, 1994.

VI. APPENDIX

The coefficients of D^*_{cl} as functions of the elements of $\mathbf{K}^*$ and plant parameters are given below:

$$\begin{aligned}
&a^*_{cl,5} = m_1 m_2, \;\; a^*_{cl,4} = m_1\left(K^*_{25} + b_2 + c\right) + m_2\left(K^*_{14} + b_1 + c\right),\\
&a^*_{cl,3} = K^*_{14}\left(b_2 + c + K^*_{25}\right) + K^*_{24}\left(c - K^*_{15}\right) + K^*_{15}c + K^*_{25}\left(b_1 + c\right)\cdots\\
&\qquad + m_1\left(K^*_{23} + k\right) + m_2\left(K^*_{12} + k\right) + \left(b_1 + b_2\right)c + b_1 b_2,\\
&a^*_{cl,2} = k\left(K^*_{14} + K^*_{15} + K^*_{24} + K^*_{25} + b_1 + b_2\right) + b_1 K^*_{23} + b_2 K^*_{12}\cdots\\
&\qquad + m_1 K^*_{21} + c\left(K^*_{12} + K^*_{13} + K^*_{22} + K^*_{23}\right) + K^*_{12}K^*_{25}\cdots\\
&\qquad - K^*_{13}K^*_{24} + K^*_{14}K^*_{23} - K^*_{15}K^*_{22},\\
&a^*_{cl,1} = k\left(K^*_{12} + K^*_{13} + K^*_{22} + K^*_{23}\right) + c\left(K^*_{11} + K^*_{21}\right) + b_1 K^*_{21}\cdots\\
&\qquad - K^*_{11}K^*_{24} + K^*_{12}K^*_{23} - K^*_{13}K^*_{22} + K^*_{14}K^*_{21},\\
&a^*_{cl,0} = k\left(K^*_{11} + K^*_{21}\right) - K^*_{11}K^*_{22} + K^*_{12}K^*_{21}.
\end{aligned} \tag{37}$$

Fig. 14 shows the energy vs. K_{ff} plot generated based on a desired position trajectory, x_d, of stroke 15 mm, with kinematic limits of 100 mm/s, 1×10^3 mm/s^2, 5×10^4 mm/s^3 and 1×10^7 mm/s^4 for velocity, acceleration, jerk and snap, respectively. Just as in Fig. 8, there is initially a sharp drop in energy as K_{ff} is increased and ringing is reduced. However, in Fig. 14 there are three local minima at K_{ff} = 66, 200 and 500; beyond K_{ff} = 500, the energy begins to increase slightly but steadily. The difference in the energy vs. K_{ff} profiles of Fig. 8 and Fig. 14 is because the trajectory used in Fig. 14 is less aggressive than that used in Fig. 8. Therefore, it has is less ringing due to poorly damped poles, and its efficiency is hurt rather than helped by having very high values of K_{ff}. This is because, in theory (i.e., in the absence of ringing), efficiency should decrease as K_{ff} increases. Nonetheless, just as in Fig. 8, as long as K_{ff} is high enough to provide sufficiently damped poles in G^{-1}_{ff-neo}, the efficiency of the proposed NEO FF remains near its optimal value, irrespective of the value of K_{ff}.

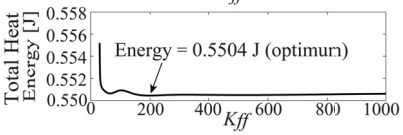

Fig. 14. Total Heat Energy of Proposed NEO FF as a Function of K_{ff} (based on Reference Trajectory given in Appendix)